J. Fluid Mech. (2022), *vol*. 937, A8, doi:10.1017/jfm.2022.94

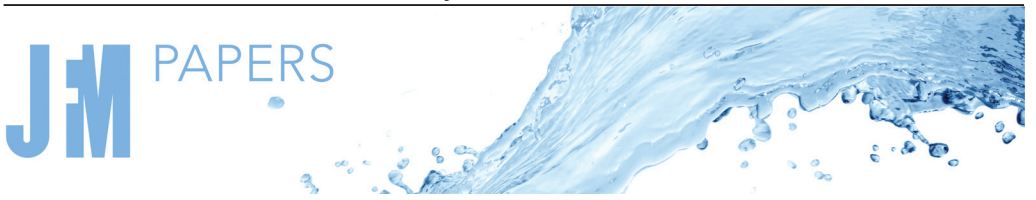

Weakly nonlinear theory for dispersive waves generated by moving seabed deformation

S. Michele[1],†, E. Renzi[2], A.G.L. Borthwick[1], C. Whittaker[3] and A.C. Raby[1]

[1]School of Engineering, Computing and Mathematics, University of Plymouth, Drake Circus, Plymouth PL4 8AA, UK

[2]Department of Mathematical Sciences, Loughborough University, Loughborough LE11 3TU, UK

[3]Department of Civil and Environmental Engineering, University of Auckland, Auckland 1010, New Zealand

(Received 7 June 2021; revised 14 November 2021; accepted 25 January 2022)

We present a weakly nonlinear theory for the evolution of dispersive transient waves generated by moving seabed deformation. Using a perturbation expansion up to second order, we show that higher-order components affect mostly the leading wave and the region close to the deforming seabed. In particular, the leading wave in the nonlinear regime has higher crests and deeper troughs than the known linear solution, while the trough that propagates together with the moving seabed exhibits pulsating behaviour and has larger depth. We also validate the analytical model with experimental data and obtain good agreement between both approaches. Our results suggest a need to extend existing models that neglect the effects of wave dispersion and higher-order components, especially in view of practical applications in engineering and oceanography.

Key words: wave-structure interactions, coastal engineering

1. Introduction

In this paper, we elucidate the role and importance of nonlinear components in the propagation of dispersive waves generated by moving seabed deformation. Our results provide a theoretical basis for applications to landslide tsunami generation and propagation.

Landslide tsunamis are induced by the motion of subaerial or submerged masses, usually localised at the margins of water bodies, e.g. oceans and lakes (Sammarco & Renzi 2008; Renzi & Sammarco 2010, 2012; Couston, Mei & Alam 2015; Renzi & Sammarco 2016). Landslide tsunamis are different from earthquake tsunamis (Fraser *et al.* 2013), as they are characterised by a more localised generation mechanism, which results in the landslide

† Email address for correspondence: simone.michele@plymouth.ac.uk

tsunami energy focussing along narrower stretches of the shoreline. This can potentially induce larger wave amplitudes than for earthquake tsunamis. Indeed, the largest recorded tsunami in human history was generated by a landslide in Lituya Bay, Alaska, which produced a runup of approximately 500 m (Kanoglou & Synolakis 2015).

Several landslide tsunami models have been developed using non-dispersive formulations for long waves, similar to those used for earthquake tsunamis (e.g. see Liu & Mei 2003; Wang, Liu & Mei 2010) and moving obstacles (Madsen & Hansen 2012). However, from a fluid dynamics point of view, landslide tsunamis are different from earthquake tsunamis because of their peculiar generation mechanism. Earthquake tsunamis are generated almost instantaneously, whereas landslide tsunamis are strongly dependent on the time history of the seafloor deformation (Lynett & Liu 2005; Sammarco & Renzi 2008). As the landslide moves, it gradually releases energy into the water. Waves are continuously generated during this process, resulting in a dispersive dynamics. Therefore, traditional non-dispersive models that are used to investigate earthquake tsunamis, often fail to reproduce the dispersive characteristics of landslide tsunamis (Cecioni & Bellotti 2010; Yavari-Ramshe & Ataie-Ashtiani 2016). Accurate modelling of landslide-generated tsunamis is critical in trying to understand past events or predict future ones. The Indonesian Palu Bay tsunami of 2018 is a case in point, where there is lack of consensus about the exact causes of the tsunami due to differences in modelling approaches (Goda *et al.* 2019).

Sammarco & Renzi (2008) showed that dispersion is responsible for shifting the maximum wave amplitude towards the middle of a wavetrain of edge waves generated by a landslide on a sloping beach. A similar effect was also described by Renzi & Sammarco (2010) for landslide tsunamis propagating around a conical island, and later confirmed experimentally by Romano, Bellotti & Risio (2013). Watts (2000) described dispersive and nonlinear features of waves generated by an idealised landslide block on a steep slope. More recently, Whittaker, Nokes & Davidson (2015) carried out physical tests using a solid mass (similar to that used by Grilli & Watts 2005) moving on an otherwise flat bed that generated a forced wave field. Their measurements confirm the importance of dispersion in shaping landslide-generated tsunamis away from the generation zone. Additional works showing the importance of dispersion on tsunami generation by three-dimensional landslides have been performed by Enet & Grilli (2007), and subsequently demonstrated by Ma, Shi & Kirby (2012) using a shock-capturing non-hydrostatic model for nonlinear free-surface wave processes.

Nonlinearity also plays an important role in the fluid dynamics of landslide tsunamis and seabed disturbances. Linearised models are only applicable if the landslide amplitude A is much smaller than the water depth h, and if the landslide speed u is smaller than the critical speed $\sqrt{gh}$, where g is the acceleration due to gravity. For example, Renzi & Sammarco (2012) and Renzi & Sammarco (2016) achieved close matches between predictions by a mathematical model based on linearised potential theory and experimental data obtained by Di Risio *et al.* (2009) for a partially submerged, thin landslide moving along an incline. However, linearised models predict incorrect wave amplitudes when the landslide is thick and nonlinear resonant amplification occurs (Liu & Mei 2003; Renzi & Sammarco 2012). Similarly, but in the context of vertical displacements, Hammack (1973) showed that the leading wave can be strongly affected by positive or negative bed displacements with behaviours showing solitary wave formation.

Computational fluid dynamics (CFD) models have been developed in recent years to investigate the dynamics of landslide tsunamis in the nonlinear regime. As described in the review by Yavari-Ramshe & Ataie-Ashtiani (2016), most CFD models solve simplified forms of the governing equations, such as the nonlinear shallow-water equations or the

higher-order Boussinesq wave equations. The vast majority of existing CFD models are based on an Eulerian approach because the more robust Lagrangian approach is computationally more expensive (Yavari-Ramshe & Ataie-Ashtiani 2016). CFD models are undoubtedly valuable tools in reproducing large-scale, realistic scenarios. However, although they can capture the key physical processes associated with wave generation by submarine mass failures (including landslides) with high spatio-temporal resolution, such models are not so convenient at providing detailed physical insight, unlike analytical models. This is because analytical models enable prediction of system behaviour at much lower computational cost, and allow parametric investigations to be conducted by manipulating analytical formulae. Analytical models may be limited by the assumptions used in their derivation, such that care should be taken in the interpretation of their results.

In this paper, we develop a combined analytical approach to elucidate the higher-order dynamics of seabed-forced dispersive waves observed in recent experiments (Whittaker *et al.* 2015). Our focus is on a seabed deformation moving over an otherwise horizontal surface rather than over an inclined slope for the following reasons. The transient wave is generated by a solid block translating with a prescribed speed, rather than purely relying on gravity. Complications are avoided from wave reflection at a sloped bed: sudden deceleration should there be an abrupt transition between an inclined and horizontal bed, and possible aquaplaning of the solid block should the transition be smooth (Sue, Nokes & Davidson 2011). On the other hand, analysis of more realistic landslides over sloping beds (or more complex bathymetries) in intermediate waters are beyond the scope of this work. A mild-slope extension of the present model may be derived to include the effects of slowly varying bathymetry. Analytical solutions can be obtained only for idealised geometries, through multiple-scale asymptotic expansion, as done by Renzi (2017) in the case of forced underwater acoustic waves. Solutions for more realistic seabed profiles require numerical techniques (Cecioni & Bellotti 2010). Numerical models are also required in the case of highly nonlinear wave generation, particularly when this leads to overturning and breaking (Capone, Panizzo & Monaghan 2010; Heller *et al.* 2016; Li, Jin & Tai 2020).

We first derive the nonlinear set of governing equations for a seafloor deformation on a flat bed. Use of an idealised geometry allows us not only to reproduce the experimental layout of Whittaker *et al.* (2015), but also to determine novel analytical solutions that explain the role of second-order terms in shaping the wave field. We solve the system of governing equations using a perturbative approach with Taylor expansions. This allows us to obtain a sequence of linearised boundary-value problems, which we solve by applying the Fourier transform in space (Mei, Stiassnie & Yue 2005). The physical meaning of the solution at each order is discussed by means of asymptotic expansions of integrals (Bender & Orszag 1999).

We show that the second-order problem is forced both at the ocean bed and on the free surface. The solution is found by decomposing each problem and separating the relevant forcing terms (Michele, Sammarco & d'Errico 2018; Michele & Renzi 2019; Michele, Renzi & Sammarco 2019). Our results reveal that these second-order components affect mostly the leading wave and the water region close to the moving seabed. Their overall effect is to increase the free-surface elevation and to generate pronounced pulsations of the wave trough above the deformation. Similar dynamics has also been noted by Whittaker *et al.* (2015) and is observed in the experimental results provided herein. We remark that the development of this weakly nonlinear theory is based on the assumption that the deformation speed is much smaller than the critical speed $\sqrt{gh}$. If the speed is close to the critical speed, resonance occurs and other analytical methods are necessary. Similar conclusions can be extended to the case of nonlinear non-dispersive waves in the presence of a steady running stream (Whitham 1974; Wu 1987; Lee, Yates & Wu 1989;

Debnath 1994), or forced by a moving bed (Dalphin & Barros 2019). Even at lower Froude numbers between 0.625 and 0.75, Whittaker *et al.* (2017) observed spilling behaviour in some of the generated waves, implying that weakly nonlinear models should be limited in application to Froude numbers less than 0.5.

The paper is structured as follows. In § 2 we discuss a second-order theory of nonlinear dispersive transient waves generated by a moving seabed deformation, based on a perturbation approach. In § 3, we present analytical second-order results that are in very satisfactory agreement with experimental data. Then in § 4 we dissect the different components of the wave field obtained with the analytical model. Asymptotic analysis allows us to identify the leading and trailing wave components at different orders. We show that the leading wave in the nonlinear regime has higher crests and deeper troughs than the known linear solution. Therefore, neglect of nonlinear effects can lead to underestimation of the maximum leading wave height. We also show that second-order effects are responsible for the development of a pulsating trough that propagates together with the bed deformation.

2. Analytical model

2.1. *Governing equations*

Let us consider the two-dimensional fluid domain Ω shown in figure 1, and assume an irrotational flow of an inviscid and incompressible fluid. As a consequence, there exists a velocity potential $\Phi(x, z, t)$, such that the velocity field $\mathbf{v} = \nabla\Phi$ where $\nabla(\cdot)$ is the nabla operator in x and z coordinates. The z axis points upwards from the undisturbed free surface, h denotes the constant offshore still water depth and $f(x, t)$ describes the elevation of the moving bed with respect to the coordinate $z = -h$; t denotes time. The governing equations for the velocity potential $\Phi(x, z, t)$ and the free-surface elevation $\zeta(x, t)$ are

$$\nabla^2\Phi = 0, \quad \Omega\,(x, z, t)\,, \tag{2.1}$$

$$\Phi_{tt} + g\Phi_z = -\,|\nabla\Phi|_t^2 - \frac{1}{2}\nabla\Phi\cdot\nabla\,|\nabla\Phi|^2\,, \quad z = \zeta, \tag{2.2}$$

$$\zeta + \frac{1}{g}\Phi_t = -\frac{1}{2g}\,|\nabla\Phi|^2\,, \quad z = \zeta, \tag{2.3}$$

$$\Phi_z - f_t = \Phi_x f_x, \quad z = -h + f, \tag{2.4}$$

$$\Phi = \Phi_t = 0, \quad z = \zeta, \quad t = 0^+, \tag{2.5}$$

where the fluid is assumed to be at rest before the bed motion initiates at $t = 0^+$, and g denotes the acceleration due to gravity. Note that the initial conditions (2.5) need simply to be prescribed on the free surface, because time derivatives of the unknowns Φ and ζ only appear in the free-surface boundary conditions. Let us introduce the following non-dimensional quantities (Mei *et al.* 2005):

$$\left.\begin{aligned}(x', z') = (x, z)/\lambda, \quad t' = t\omega, \quad \Phi' = \Phi/(A\omega\lambda),\\ (\zeta', f') = (\zeta, f)/A, \quad G' = g/(\omega^2\lambda),\end{aligned}\right\} \tag{2.6a–e}$$

where A is the amplitude of the bed disturbance which is taken to be much smaller than the typical free-surface wavelength λ, ω denotes the wave frequency and primes indicate non-dimensional variables. We introduce the following length ratio $\epsilon = A/\lambda \ll 1$, which represents the wave steepness. We also assume that λ is the length scale of the moving

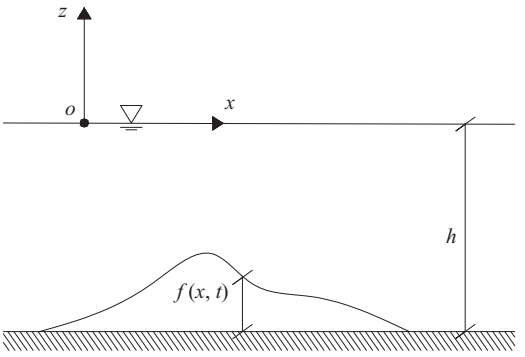

Figure 1. Side view of the moving seabed deformation system.

bed perturbation, and so the landslide steepness is of the same order ϵ as the free-surface waves. Substitution of (2.6*a–e*) into (2.1)–(2.5) yields the boundary-value problem (b.v.p.) in non-dimensional form

$$\nabla'^2\Phi' = 0, \quad \Omega(x', z', t'), \tag{2.7}$$

$$\Phi'_{t't'} + G'\Phi'_{z'} = -\epsilon\left|\nabla'\Phi'\right|^2_{t'} - \epsilon^2\tfrac{1}{2}\nabla'\Phi'\cdot\nabla'\left|\nabla'\Phi'\right|^2, \quad z' = \epsilon\zeta', \tag{2.8}$$

$$G'\zeta' + \Phi'_{t'} = -\epsilon\tfrac{1}{2}\left|\nabla'\Phi'\right|^2, \quad z' = \epsilon\zeta', \tag{2.9}$$

$$\Phi'_{z'} - f'_{t'} = \epsilon\Phi'_{x'}f'_{x'}, \quad z' = -h' + \epsilon f', \tag{2.10}$$

$$\Phi' = \Phi'_{t'} = 0, \quad z' = \epsilon\zeta', \quad t' = 0^+. \tag{2.11}$$

As a consequence all the terms on the right-hand sides of (2.1)–(2.5) are also small. The free-surface boundary conditions are evaluated noting correspondence of $z' = \epsilon\zeta'$. The boundary condition at the seabed is evaluated as $z' = -h' + \epsilon f'$. Thus Taylor expanding (2.8)–(2.10) up to $O(\epsilon)$ yields

$$\Phi'_{t't'} + G'\Phi'_{z'} = -\epsilon[\zeta'(\Phi'_{t't'z'} + G\Phi'_{z'z'}) + \left|\nabla'\Phi'\right|^2_{t'}] \quad z' = 0, \tag{2.12}$$

$$G'\zeta' + \Phi'_{t'} = -\epsilon(\zeta'\Phi'_{t'z'} + \tfrac{1}{2}\left|\nabla'\Phi'\right|^2) \quad z' = 0, \tag{2.13}$$

$$\Phi'_{z'} - f'_{t'} = \epsilon(\Phi'_{x'}f'_{x'} - f'\Phi'_{z'z'}), \quad z' = -h'. \tag{2.14}$$

Let us introduce the following expansions of the non-dimensional velocity potential and free-surface elevation:

$$\{\Phi', \zeta'\} = \{\Phi'_1, \zeta'_1\} + \epsilon\{\Phi'_2, \zeta'_2\}, \tag{2.15}$$

where the subscripts indicate the first- (leading) and second-order solutions. Use of the expansion (2.15) yields the following equations for $n = 1, 2$:
(i) Laplace equation

$$\nabla'^2\Phi'_n = 0, \quad \text{in } \Omega(x', z'). \tag{2.16}$$

(ii) Free-surface dynamic condition

$$G'\zeta' + \Phi'_{t'} = \mathcal{B}_n, \quad z' = 0, \tag{2.17}$$

where

$$\mathcal{B}_1 = 0, \quad \mathcal{B}_2 = -\zeta_1' \Phi'_{1_{t'z'}} - \tfrac{1}{2}\left|\nabla' \Phi_1'\right|^2. \tag{2.18a,b}$$

(iii) Free-surface mixed condition

$$\Phi'_{n_{t't'}} + G' \Phi'_{n_{z'}} = \mathcal{F}_n, \quad z' = 0, \tag{2.19}$$

where

$$\mathcal{F}_1 = 0, \quad \mathcal{F}_2 = -\zeta_1' (\Phi'_{1_{t't'z'}} + G' \Phi'_{1_{z'z'}}) - \left|\nabla' \Phi_1'\right|^2_{t'}. \tag{2.20a,b}$$

(iv) Boundary condition at the seabed

$$\Phi'_{z'} - f'_{t'} = \mathcal{G}_n, \quad z' = -h', \tag{2.21}$$

where

$$\mathcal{G}_1 = 0, \quad \mathcal{G}_2 = \Phi'_{1_{x'}} f'_{x'} - f' \Phi'_{1_{z'z'}}. \tag{2.22a,b}$$

(v) Initial condition

$$\Phi'_n = \Phi'_{n_{t'}} = 0, \quad z' = 0, \ \ t' = 0^+. \tag{2.23}$$

Having obtained the governing equations at each order n we are now in a position to solve each b.v.p. at the leading order $O(1)$ and second order $O(\epsilon)$.

2.2. *Leading-order problem* $O(1)$

Returning back to physical variables we get the following leading-order problem:

$$\nabla^2 \Phi_1 = 0, \quad \Omega\,(x, z)\,, \tag{2.24}$$

$$\Phi_{1_{tt}} + g \Phi_{1_z} = 0, \quad z = 0, \tag{2.25}$$

$$\zeta_1 + \frac{1}{g} \Phi_{1_t} = 0, \quad z = 0, \tag{2.26}$$

$$\Phi_{1_z} = f_t, \quad z = -h, \tag{2.27}$$

$$\Phi_1 = \Phi_{1_t} = 0, \quad z = 0, \ \ t = 0^+. \tag{2.28}$$

By applying the Fourier transform along the x coordinate, solving the b.v.p. via separation of variables and transforming back to the spatial variable, we obtain the following expression for the velocity potential:

$$\Phi_1 = -\frac{1}{2\pi} \int_0^t \mathrm{d}\tau \int_{-\infty}^{\infty} \frac{g \cosh\left[k\,(h+z)\right] \hat{W}\,(t, k) \sin\left[\omega\,(\tau - t)\right] \mathrm{e}^{\mathrm{i}kx}}{\omega \cosh^2(kh)} \,\mathrm{d}k + \frac{1}{2\pi} \int_{-\infty}^{\infty} \frac{\hat{W}\,(t, k)\, \mathrm{e}^{\mathrm{i}kx} \sinh(kz)}{k \cosh(kh)} \,\mathrm{d}k, \tag{2.29}$$

and the free-surface elevation

$$\zeta_1 = \frac{1}{2\pi} \int_0^t \mathrm{d}\tau \int_{-\infty}^{\infty} \frac{\hat{W}\,(\tau, k)\, \mathrm{e}^{\mathrm{i}kx} \cos\left[\omega\,(\tau - t)\right]}{\cosh(kh)} \,\mathrm{d}k, \quad \omega^2 = gk \tanh(kh), \tag{2.30}$$

where we use the shorthand notation $W(x,\tau)=f_\tau$, so that

$$\hat{W}(\tau,k)=\int_{-\infty}^{\infty} f_\tau\,\mathrm{e}^{-\mathrm{i}kx}\,\mathrm{d}x \tag{2.31}$$

is the associated Fourier transform. As an example, let us consider the following analytical expression for the bed perturbation:

$$f(x,t)=A\exp(-\sigma[x-utH(t)]^2), \tag{2.32}$$

in which u is the horizontal speed, σ is a shape factor, A is the maximum thickness of the perturbed bed and $H(t)$ is the Heaviside step function. Then

$$f_\tau=2Au\sigma\,[x-u\tau H(\tau)]\exp(-\sigma[x-u\tau H(\tau)]^2)H(\tau)\,, \tag{2.33}$$

and (2.31) becomes

$$\hat{W}(\tau,k)=-\frac{\mathrm{i}Aku\sqrt{\pi}\exp(-[k(k+4\mathrm{i}\tau u\sigma)/(4\sigma)])H(\tau)}{\sqrt{\sigma}}. \tag{2.34}$$

Substitution of (2.34) into (2.30) yields finally

$$\Phi_1=-\frac{g}{2\pi}\int_{-\infty}^{\infty}\frac{\mathrm{e}^{\mathrm{i}kx}\cosh[k(h+z)]}{\omega\cosh^2(kh)}S(k,t)\,\mathrm{d}k+\frac{1}{2\pi}\int_{-\infty}^{\infty}\frac{\hat{W}(t,k)\,\mathrm{e}^{\mathrm{i}kx}\sinh(kz)}{k\cosh(kh)}\,\mathrm{d}k, \tag{2.35}$$

$$\zeta_1=\frac{1}{2\pi}\int_{-\infty}^{\infty}\frac{\mathrm{e}^{\mathrm{i}kx}}{\cosh(kh)}C(k,t)\,\mathrm{d}k, \tag{2.36}$$

where the terms C and S are, respectively,

$$C(k,t)=-\frac{\mathrm{i}Aku\sqrt{\pi}\,\mathrm{e}^{-k^2/(4\sigma)}[\mathrm{i}\,\mathrm{e}^{-\mathrm{i}ktu}ku-\mathrm{i}ku\cos(\omega t)-\omega\sin(\omega t)]}{(k^2u^2-\omega^2)\sqrt{\sigma}}, \tag{2.37}$$

$$S(k,t)=-\frac{\mathrm{i}Aku\sqrt{\pi}\,\mathrm{e}^{-k^2/(4\sigma)}[-\mathrm{e}^{-\mathrm{i}ktu}\omega+\omega\cos(\omega t)-\mathrm{i}ku\sin(\omega t)]}{(k^2u^2-\omega^2)\sqrt{\sigma}}. \tag{2.38}$$

Note that $C(-k,t)=\bar{C}(k,t)$ and $S(-k,t)=\bar{S}(k,t)$, where the bar denotes the complex conjugate, hence the integrals in (2.35)–(2.36) are real. They can be evaluated numerically, and the approximation investigated asymptotically for large times and distance from $x=0$, as described in § 4. Use of (2.36)–(2.37) yields the following analytical expression of the free-surface elevation in integral form:

$$\zeta_1=-\frac{\mathrm{i}Au}{2\sqrt{\pi\sigma}}\int_{-\infty}^{\infty}\frac{k\exp(\mathrm{i}kx-k^2/(4\sigma))[\mathrm{i}\,\mathrm{e}^{-\mathrm{i}ktu}ku-\mathrm{i}ku\cos(\omega t)-\omega\sin(\omega t)]}{(k^2u^2-\omega^2)\cosh(kh)}\mathrm{d}k. \tag{2.39}$$

2.3. *Second-order problem $O(\epsilon)$*

The second-order problem expressed in terms of physical variables is given by

$$\nabla^2 \Phi_2 = 0, \quad \Omega\,(x, z)\,, \tag{2.40a,b}$$

$$\Phi_{2_{tt}} + g\Phi_{2_z} = -\frac{1}{\epsilon}[\zeta_1(\Phi_{1_{tz}} + g\Phi_{1_{zz}}) - 2g\Phi_{1_x}\zeta_{1_x} + 2\Phi_{1_{zt}}\zeta_{1_t}] = F\,(x, t)\,, \quad z = 0, \tag{2.41}$$

$$\zeta_2 + \frac{1}{g}\Phi_{2_t} = -\frac{1}{\epsilon}\left[\frac{1}{2g}(\Phi_{1_x}^2 + \zeta_{1_t}^2) + \frac{\Phi_{1_{zt}}\zeta_1}{g}\right] = B\,(x, t)\,, \quad z = 0, \tag{2.42}$$

$$\Phi_{2_z} = \frac{1}{\epsilon}(-\Phi_{1_{zz}} f + \Phi_{1_x} f_x) = G\,(x, t)\,, \quad z = -h, \tag{2.43}$$

$$\Phi_2 = \Phi_{2_t} = 0, \quad z = 0, \quad t = 0^+. \tag{2.44}$$

To determine the free-surface elevation ζ_2, we decompose the second-order velocity potential as $\Phi_2 = \Phi_F + \Phi_G$, where Φ_F represents the solution forced at the free surface, while Φ_G represents the solution forced by the bed motion. This implies that $f(x, t)$ cannot have edges leading to infinite velocity, because the second-order solution would otherwise become unbounded. In addition, we decompose the free-surface elevation ζ_2 into three components, namely $\zeta_2 = \zeta_F + \zeta_G + B$, where $B = B(x, t)$ represents the second-order forcing of the first-order solution, defined in (2.42). For later convenience, we include all the components of each forcing term G, F and B, in Appendix A.

We now proceed to solve each component separately.

2.3.1. *Second-order free-surface forcing term*

The set of governing equations is given by

$$\nabla^2 \Phi_F = 0, \quad \Omega\,(x, z)\,, \tag{2.45}$$

$$\Phi_{F_{tt}} + g\Phi_{F_z} = F\,(x, t)\,, \quad z = 0, \tag{2.46}$$

$$\zeta_F + \frac{1}{g}\Phi_{F_t} = 0, \quad z = 0, \tag{2.47}$$

$$\Phi_{F_z} = 0, \quad z = -h, \tag{2.48}$$

$$\Phi_F = \Phi_{F_t} = 0, \quad z = 0, \quad t = 0^+. \tag{2.49}$$

A solution can be sought by applying the Fourier transform along the x coordinate. We obtain

$$\Phi_F = \frac{1}{2\pi}\int_0^t \int_{-\infty}^{\infty} \frac{\cosh\left[k\,(h + z)\right]\hat{F}\,(\tau, k)\,\mathrm{e}^{\mathrm{i}kx}\sin\left[\omega\,(\tau - t)\right]}{\omega\cosh(kh)}\mathrm{d}k\,\mathrm{d}\tau, \tag{2.50}$$

where $\hat{F}(t, k)$ is the Fourier transform of the forcing term on the free surface (see (2.41)).

By applying the Leibniz integral rule to (2.50), we obtain the free-surface elevation ζ_F given by the effect of the forcing terms on the free surface:

$$\zeta_F(x,t) = -\frac{1}{2g\pi}\int_0^t\int_{-\infty}^{\infty}\int_{-\infty}^{\infty} F(\tau,\xi)\exp(-\mathrm{i}k(\xi-x))\cos[\omega(\tau-t)]\,\mathrm{d}\xi\,\mathrm{d}k\,\mathrm{d}\tau. \tag{2.51}$$

The latter can be evaluated numerically for given values of the horizontal coordinate x and time t.

2.3.2. *Second-order bed forcing term*

The b.v.p. is

$$\nabla^2\Phi_G = 0, \quad \Omega(x,z,t), \tag{2.52}$$

$$\Phi_{G_{tt}} + g\Phi_{G_z} = 0, \quad z = 0, \tag{2.53}$$

$$\zeta_G + \frac{1}{g}\Phi_{G_t} = 0, \quad z = 0, \tag{2.54}$$

$$\Phi_{G_z} = G(x,t), \quad z = -h, \tag{2.55}$$

$$\Phi_G = \Phi_{G_t} = 0, \quad z = 0, \quad t = 0^+. \tag{2.56}$$

The solution is formally equivalent to that derived at leading order. We obtain the forced second-order potential,

$$\Phi_G = -\frac{1}{2\pi}\int_0^t\int_{-\infty}^{\infty}\frac{g\cosh[k(h+z)]\hat{G}(t,k)\,\mathrm{e}^{\mathrm{i}kx}\sin[\omega(\tau-t)]}{\omega\cosh^2(kh)}\mathrm{d}k\,\mathrm{d}\tau + \frac{1}{2\pi}\int_{-\infty}^{\infty}\frac{\hat{G}(t,k)\,\mathrm{e}^{\mathrm{i}kx}\sinh(kz)}{k\cosh(kh)}\mathrm{d}k, \tag{2.57}$$

where $\hat{G}$ is the Fourier transform of the forcing term at the bed, $G(x,t)$.

Similar to the previous section, the corresponding free-surface elevation is derived upon application of the Leibniz integral rule, which yields

$$\zeta_G(x,t) = \frac{1}{2\pi}\int_0^t\int_{-\infty}^{\infty}\int_{-\infty}^{\infty}\frac{G(\tau,\xi)\exp(-\mathrm{i}k(\xi-x))\cos[\omega(\tau-t)]}{\cosh(kh)}\mathrm{d}\xi\,\mathrm{d}k\,\mathrm{d}\tau. \tag{2.58}$$

The sought solution for the free-surface elevation is given by

$$\zeta(x,t) = \zeta_1(x,t) + \epsilon[\zeta_F(x,t) + \zeta_G(x,t) + B(x,t)] + O(\epsilon^2). \tag{2.59}$$

3. Validation

In this section, we validate the analytical model with experimental data for a block moving along a horizontal boundary. The experimental set-up is the same as utilised by Whittaker *et al.* (2015) and is summarised briefly in § 3.1. However, the motion of the model landslide excludes the block deceleration phase, to facilitate comparisons with the theoretical model assumptions outlined in § 2.

3.1. *Experimental set-up*

Experiments were undertaken in a flume of 0.25 m width and 14.66 m length. Waves were generated by a semi-ellipsoidal moving block of length $L = 0.5$ m and height $A = 0.026$ m sliding on a horizontal seabed, at a depth $h = 0.175$ m. Use of a horizontal boundary and the location of the block near the centre of the flume (i.e. approximately equidistant from the flume ends) ensured that waves propagating in both positive and negative directions could be measured prior to reflection. No wave absorption material was present at the ends of the flume. The experimental set-up is described in detail by Whittaker *et al.* (2015).

The block motion (provided by a servo motor) comprised an initial acceleration at a constant rate $a_0 = 1.5\,\mathrm{m\,s^{-2}}$ until $t = 0.109$ s, when the block reached its maximum velocity of $u = 0.164\,\mathrm{m\,s^{-1}}$. This is similar to Run 5 reported by Whittaker *et al.* (2015), and corresponds to a landslide Froude number of 0.125. However, in the experiments undertaken by Whittaker *et al.* (2015), the landslide moved at its maximum velocity for 2.00 s before decelerating to rest (with a deceleration of $-a_0$). In these experiments, the landslide block did not decelerate during the measurement period. In other words, the block motion consisted of an initial rapid acceleration followed by a long period of constant velocity. Whittaker *et al.* (2017) present a similar wave field for a Froude number of 0.5, but did not include wave fields generated at lower Froude numbers. The rapid block acceleration, relatively low maximum velocity (i.e. Froude number) and lack of deceleration make these experimental results suitable for theoretical comparisons because the block movement matches the assumptions in (2.32).

In the experiments carried out by Whittaker *et al.* (2015, 2017), free-surface elevations were measured within a spatial window of approximately 0.35 m using a laser-induced fluorescence technique to an accuracy of ± 4 mm. The highly repeatable block motion allowed the full wave field to be measured through 37 repetitions of the experiment, ensuring some overlap between adjacent fields of view to create a continuous free-surface record.

3.2. *Analytical vs experimental results*

Now we compare analytical results with data from the experimental campaign outlined above. Water depth and landslide velocity are the same as in the previous section, the bed deformation maximum thickness is $A = 0.026$ m and the shape factor representing the moving block is $\sigma = 19\,\mathrm{m^{-2}}$. Although subtle differences exist between the shape of the block in the experiments and analytical model, previous research (e.g. Sue *et al.* 2011; Whittaker *et al.* 2015) has demonstrated that acceptable agreement can be obtained if the volumes are equal. The analytical domain also extends to infinity on both sides, whereas the experimental set-up is 14.66 m long. Figure 2 shows snapshots of the free-surface elevation ζ obtained with the second-order and leading-order models. On the same figure the free-surface elevation evaluated experimentally (dashed line) is also plotted. A pronounced leading wave travels ahead of the solid block, while a trough propagates in the opposite direction. Both waves are followed by trailing wave packets that resemble the Airy wave solution discussed later in § 4. The times of arrival of crests and troughs, as well as the overall shape of the wave patterns are in close agreement between the two models. Slight differences in the profiles appear at small times, where the leading wave and the trough are underestimated by the analytical model. Note that at small times the dynamics is highly nonlinear, as the bed deformation imparts a sudden impulse to the surrounding fluid when its speed changes from $u = 0$ for $t < 0$ to $u > 0$ for $t \geq 0$. Also, the moving block velocity in the experimental set-up increases gradually until $t = 0.109$ s,

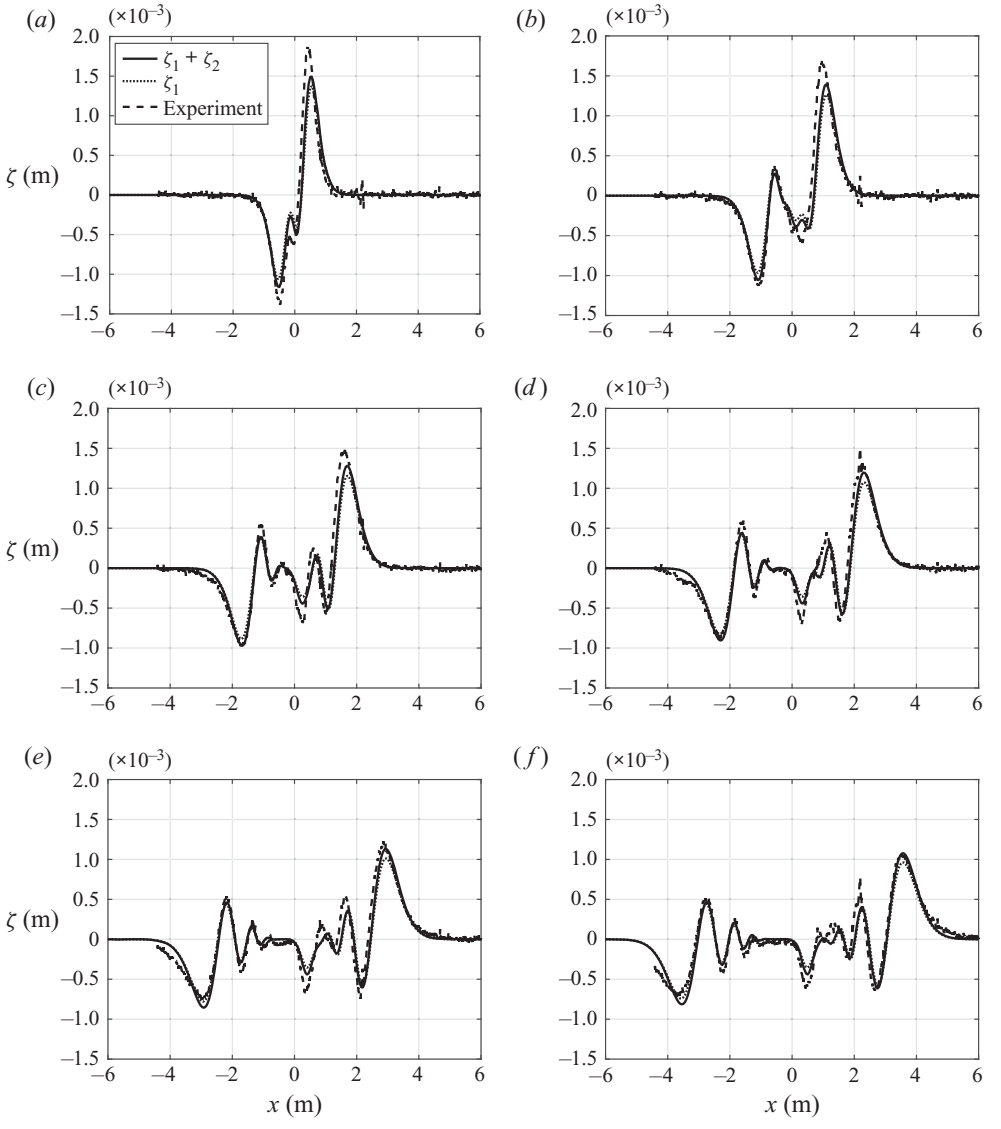

Figure 2. Second-order free-surface elevation $\zeta_2 + \zeta_1$, leading-order free-surface elevation ζ_1 and experimental data at times: (*a*) $t = 0.5$ s, (*b*) $t = 1$ s, (*c*) $t = 1.5$ s and (*d*) $t = 2$ s, (*e*) $t = 2.5$ s and (*f*) $t = 3$ s. The agreement between the models is good with few discrepancies at the initial stage. This is likely due to the instantaneous acceleration not possible in the experimental set-up.

whereas the velocity of the moving bed slide for the theoretical model is described by the Heaviside step function as shown by (2.32). Therefore, the small differences between the analytical and experimental models (i.e. the over-estimation of wave amplitudes in the second-order solution) are likely due to the effects highlighted above. Interestingly, the leading-order solution ζ_1 still underestimates the amplitudes of the generated waves, despite the instantaneous acceleration assumed in this model, reinforcing the importance of the second-order contributions to the generated wave field. Note also that at large times there are discrepancies in front of the leftward propagating trough. This is due to the near-complete wave reflection caused by the presence of the vertical wall on the

left side of the channel flume, whereas the fluid domain for the analytical model extends toinfinity. Reflections from this boundary were first observed at approximately $t = 1.6$ s in the physical experiments (Whittaker *et al.* 2015).

4. Wave field analysis

Having validated the analytical model, we now discuss the characteristic features of the wave field generated by the motion of the seabed. The analytical solution given in § 2 is instrumental to elucidating the role of the first- and second-order contributions.

4.1. *Rightward leading wave at first order*

In this section we derive the profile of the rightward leading wave; the asymptotic behaviour of the leftward propagating trough can be found in a similar manner.

First, we note that the contribution given by the first term within the square brackets in (2.39) is negligible, because the integral has no stationary points (Mei *et al.* 2005). The free-surface elevation at large distances can consequently be approximated as

$$\begin{aligned}\zeta_1^{\infty} &\simeq -\frac{Au}{\sqrt{\pi\sigma}}\int_0^{\infty}\frac{\exp(-k^2/(4\sigma))[k^2u\cos kx\cos(\omega t)+\omega k\sin kx\sin(\omega t)]}{(k^2u^2-\omega^2)\cosh(kh)}\mathrm{d}k\\ &= -\frac{Au}{2\sqrt{\pi\sigma}}Re\int_0^{\infty}\frac{\exp(-k^2/(4\sigma))[k^2u\,(\exp(\mathrm{i}\,(kx-\omega t))+\exp(\mathrm{i}\,(kx+\omega t)))}{(k^2u^2-\omega^2)\cosh(kh)}\\ &\qquad\frac{+\omega k\,(\exp(\mathrm{i}\,(kx-\omega t))-\exp(\mathrm{i}\,(kx+\omega t)))]}{}\mathrm{d}k.\end{aligned} \tag{4.1}$$

The first and second terms within each round bracket of the numerator represent rightward and leftward propagating waves, respectively. Given that rightward leading waves are located at $x > 0$, the integral including $\exp\{\mathrm{i}(kx+\omega t)\}$ does not have a stationary point and provides a negligible contribution (Bender & Orszag 1999). Hence, only the integral including the first complex exponential $\exp\{\mathrm{i}(kx-\omega t)\}$ is of significance. We obtain

$$\begin{aligned}\zeta_1^{\infty} &\simeq -\frac{Au}{2\sqrt{\pi\sigma}}Re\int_0^{\infty}\frac{k\exp(-k^2/(4\sigma)+\mathrm{i}\,(kx-\omega t))(ku+\omega)}{(k^2u^2-\omega^2)\cosh(kh)}\mathrm{d}k\\ &= \int_0^{\infty}\tilde{\zeta}(k)\cos(kx-\omega t)\,\mathrm{d}k.\end{aligned} \tag{4.2}$$

Note that leading waves move at speeds close the shallow-water celerity $\sqrt{gh}$ and correspond to small wavenumbers $k \sim 0$. To investigate the latter integral analytically, let us expand ω about $k \to 0$ and take into account wave dispersion up to the third power:

$$\omega \simeq \sqrt{gh}k\left(1-\frac{h^2k^2}{6}\right). \tag{4.3}$$

Substitution of (4.3) into (4.2) yields

$$\zeta_1^{\infty} \simeq \int_0^{\infty}\tilde{\zeta}(k)\cos\left[k\big(x-t\sqrt{gh}\big)+k^3\frac{\sqrt{gh}h^2t}{6}\right]\mathrm{d}k. \tag{4.4}$$

The latter integral can be further simplified by Taylor expanding $\tilde{\zeta}$ about $k \to 0$ and considering the first-order term (Whitham 1974; Debnath 1994; Mei *et al.* 2005)

$$\zeta_1^{\infty} \simeq \frac{Au}{2\big(\sqrt{gh}-u\big)\sqrt{\pi\sigma}}\int_0^{\infty}\cos\left[k\big(x-t\sqrt{gh}\big)+\frac{th^2k^3\sqrt{gh}}{6}\right]\mathrm{d}k. \tag{4.5}$$

Let us now substitute the following variables:

$$Z\alpha = k\big(x - \sqrt{gh}t\big), \quad Z^3 = \frac{2\big(x - \sqrt{gh}t\big)^3}{\sqrt{gh}h^2t}. \tag{4.6a,b}$$

This yields

$$\zeta_1^{\infty} \simeq \frac{A\sqrt{\pi}Fr}{2\,(1-Fr)\,\sqrt{\sigma}} \left(\frac{2}{h^2t\sqrt{gh}}\right)^{1/3} \mathrm{Ai}\left[\left(\frac{2}{h^2t\sqrt{gh}}\right)^{1/3}\left[x - t\sqrt{gh}\right]\right], \tag{4.7}$$

where Ai is Airy's function and $Fr = u/\sqrt{gh}$ is the Froude number of the disturbance. For an observer travelling at a speed close to the long-wave speed $\sqrt{gh}$, the leading wave ζ_1^{∞} decays as $O(t^{-1/3})$. This rate of decay is the same as that of transient waves generated by an initial displacement of the free surface (Mei *et al.* 2005).

Note that (4.7) is proportional to the volume of the disturbance $A\sqrt{\pi}/\sqrt{\sigma}$, and that it becomes unbounded as $Fr \to 1$, i.e. as the disturbance speed tends to the wave speed in shallow water $\sqrt{gh}$. The same result is also obtained in the case of surface waves on a running stream and has been investigated by several authors (Whitham 1974; Wu 1987; Lee *et al.* 1989; Debnath 1994).

4.2. *Free-surface elevation in the disturbance region at the leading order*

To analyse the free-surface elevation in the disturbance region behind the leading wave, let us split (2.39) into two components, $\zeta_1 = \zeta_1^s + \zeta_1^w$, where ζ_1^s represents a stationary free-surface elevation in the moving reference frame $X = x - ut$, and ζ_1^w denotes an oscillating part.

Let us start with the stationary component, i.e.

$$\zeta_1^s = \frac{Au^2}{2\sqrt{\pi\sigma}} \int_{-\infty}^{\infty} \frac{k^2 \exp(\mathrm{i}kX - k^2/(4\sigma))}{(k^2u^2 - \omega^2)\cosh(kh)}\mathrm{d}k. \tag{4.8}$$

The latter integral cannot be investigated via the stationary phase method because the term X is insufficiently large in the landslide region. However, the integral can be investigated analytically by noting that the term $\exp\{-k^2/(4\sigma)\}$ governs the leading behaviour of the integrand in $k \sim 0$. Hence, by Taylor expanding the integrand about $k \to 0$, except for the exponential terms, we obtain

$$\zeta_1^s \simeq -\frac{Au^2}{2\sqrt{\pi\sigma}(gh - u^2)} \int_{-\infty}^{\infty} \exp(\mathrm{i}kX - k^2/(4\sigma))\,\mathrm{d}k = -\frac{Au^2\,\mathrm{e}^{-X^2\sigma}}{(gh - u^2)} = -\frac{f(X)Fr^2}{(1 - Fr^2)}. \tag{4.9}$$

Retaining the exponential terms, instead of including them in the Taylor expansion, allows us to find the dependence on the moving coordinate X and to improve the accuracy of the approximated solution of (4.9). From (4.9) we note that the solution becomes unbounded as $Fr \to 1$, whereas if the seabed velocity is smaller than the wave speed in shallow water, i.e. $Fr < 1$, the free-surface elevation develops a trough of permanent shape moving with the seabed deformation at speed u. This result for the first-order stationary component ζ_1^s is identical to the well-known result for long waves (Levin & Nosov 2016). Similar behaviour has also been observed experimentally by Whittaker *et al.* (2015) and in the experimental results provided in figure 2.

The oscillating part ζ_1^w can be investigated by using the method of stationary phase (Mei *et al.* 2005). From (4.2) we obtain

$$\zeta_1^w = -\frac{Au}{2\sqrt{\pi\sigma}} Re \int_0^\infty \frac{k \exp(-k^2/(4\sigma) + \mathrm{i}\,(kx - \omega t))(ku + \omega)}{(k^2u^2 - \omega^2)\cosh(kh)} \mathrm{d}k$$
$$\simeq -\frac{Au}{\sqrt{2\sigma t\,|\omega_0''|}} \frac{k_0 \exp(-k_0^2/(4\sigma))}{(k_0u - \omega_0)\cosh(k_0h)} \cos\left(k_0x - \omega_0 t + \frac{\pi}{4}\right), \tag{4.10}$$

where k_0 is the stationary point satisfying $x/t = \mathrm{d}\omega/\mathrm{d}k$, and ω_0 is the frequency evaluated at k_0. For deeper physical insight, let us now consider the Boussinesq expansion (4.3) and consider an observer moving together with the bed deformation, i.e. $x = ut$. The explicit expressions for k_0 and $\omega_0'' = \mathrm{d}^2\omega/\mathrm{d}k^2|_{k_0}$ simplify as

$$k_0 = \frac{\sqrt{2\,(1 - Fr)}}{h}, \quad \omega_0'' = -h^2k_0\sqrt{gh} = -h\sqrt{2gh\,(1 - Fr)}, \tag{4.11a,b}$$

respectively. Substituting (4.11*a*,*b*) back into (4.10), we obtain

$$\zeta_1^w \simeq \frac{3Au \exp(-k_0^2/(4\sigma))}{2^{7/4}\,(1 - Fr)^{5/4}\,(gh)^{3/4}\,\sqrt{\sigma ht}\cosh(k_0h)} \cos\left[\frac{2t\sqrt{2gh}\,(1 - Fr)^{3/2}}{3h} - \frac{\pi}{4}\right], \tag{4.12}$$

i.e. the observer sees a train of waves decaying as $O(t^{-1/2})$ and travelling rightwards along the trough (4.9), with relative phase speed

$$c = u - \frac{\omega_0}{k_0} = \frac{2\sqrt{gh}}{3}\,(1 - Fr)\,. \tag{4.13}$$

Note that as $t \to \infty$ only the stationary component ζ_1^s survives.

As outlined by Schäffer & Madsen (1995) and Kirby (2016), the expansion (4.3) can be further improved to approximate the frequency ω even in the case of large wavenumber k. However, the stationary point k_0 would not have an explicit expression anymore and numerical methods are required to evaluate the solution. Given that our scope is to find explicit, approximate expressions for the free-surface elevation, we retain terms up to third order and continue to adopt the classical Boussinesq expansion (4.3).

4.3. *Second-order term ζ_G*

To investigate the behaviour of the forcing term G inside the expression for ζ_G (2.58), we first analyse the component $\Phi_{zz}f$, where Φ_{zz} is defined by (A7) and f represents the bed deformation (2.32). The shape function f is governed by an exponential term associated with forcing in the landslide region $X \sim 0$, and so we expect that oscillatory components far from the perturbation make small contributions. The steady component in Φ_{zz} reads

$$\Phi_{1_{zz}} = -\frac{\mathrm{i}Au}{2\sqrt{\pi\sigma}} \int_{-\infty}^{\infty} \frac{k^3 \exp(\mathrm{i}k(x - ut) - k^2/(4\sigma))}{(k^2u^2 - \omega^2)\cosh^2(kh)} \mathrm{d}k$$
$$+ \frac{\mathrm{i}Au}{2g\sqrt{\pi\sigma}} \int_{-\infty}^{\infty} k\omega^2 \exp(\mathrm{i}k(x - ut) - k^2/(4\sigma))\,\mathrm{d}k. \tag{4.14}$$

The latter integrals can be investigated analytically by noting that the exponential $\exp\{-k^2/(4\sigma)\}$ focuses the contributions as $k \to 0$. As before, we retain the complex

exponential to improve the approximation, but Taylor expand the other terms about $k \to 0$. Hence,

$$\begin{aligned}\Phi_{1_{zz}} &\simeq -\frac{\mathrm{i}Au}{2\sqrt{\pi\sigma}(u^2-gh)}\int_{-\infty}^{\infty} k\exp(\mathrm{i}k(x-ut)-k^2/(4\sigma))\,\mathrm{d}k \\ &\quad+\frac{\mathrm{i}Auh}{2\sqrt{\pi\sigma}}\int_{-\infty}^{\infty} k^3\exp(\mathrm{i}k(x-ut)-k^2/(4\sigma))\,\mathrm{d}k \\ &= -\frac{2f(X)u\sigma X}{h}\left\{\frac{1}{1-Fr^2}+2h^2\sigma[3-2\sigma X^2]\right\}, \end{aligned} \tag{4.15}$$

which models a rightwards propagating trough followed by a single crest. Similarly, we derive the steady component of Φ_x (A8) which is part of the forcing term $\Phi_x f_x$ in G as

$$\begin{aligned}\Phi_{1_x} &= -\frac{Aug}{2\sqrt{\pi\sigma}}\int_{-\infty}^{\infty}\frac{k^2\exp(\mathrm{i}k(x-ut)-k^2/(4\sigma))}{(k^2u^2-\omega^2)\cosh^2(kh)}\mathrm{d}k \\ &\quad-\frac{Au}{2g\sqrt{\pi\sigma}}\int_{-\infty}^{\infty}\omega^2\exp(\mathrm{i}k(x-ut)-k^2/(4\sigma))\,\mathrm{d}k. \end{aligned} \tag{4.16}$$

Again, we retain the complex exponential and Taylor expand the integrands about $k \to 0$,

$$\begin{aligned}\Phi_{1_x} &\simeq -\frac{Aug}{2\sqrt{\pi\sigma}(u^2-gh)}\int_{-\infty}^{\infty}\exp(\mathrm{i}k(x-ut)-k^2/(4\sigma))\,\mathrm{d}k \\ &\quad-\frac{Auh}{2\sqrt{\pi\sigma}}\int_{-\infty}^{\infty}k^2\exp(\mathrm{i}k(x-ut)-k^2/(4\sigma))\,\mathrm{d}k \\ &= -\frac{f(X)u}{h}\left\{\frac{1}{1-Fr^2}+2h^2\sigma[1-2\sigma X^2]\right\}, \end{aligned} \tag{4.17}$$

which represents a propagating trough. Therefore, the forcing term G (2.43) can be approximated as

$$G \simeq \frac{4u\sigma f^2 X[1+4h^2\sigma(1-Fr^2)(1-\sigma X^2)]}{\epsilon h(1-Fr^2)}. \tag{4.18}$$

Use of the expression for ζ_G (2.58) yields

$$\zeta_G = \frac{A}{8\pi\sqrt{2}h(1-Fr^2)}\int_{-\infty}^{\infty}\frac{\exp(\mathrm{i}kx+k^2/(8\sigma))C}{\cosh(kh)}[4+h^2(1-Fr^2)(k^2+4\sigma)]\mathrm{d}k. \tag{4.19}$$

Let us first define the rightward leading wave approximation of the term above as ζ_G^{∞}. By expanding the integrand except for the phase functions and recalling that terms proportional to $\exp\{\mathrm{i}(kx+\omega t)\}$ give negligible contributions we obtain

$$\begin{aligned}\zeta_G^{\infty} &\simeq -\frac{A^2[hu^2\sigma-g(1+h^2\sigma)]}{2\sqrt{2\pi\sigma}(u^2-gh)^2}\int_0^{\infty}\cos(kx-\omega t)\mathrm{d}k \\ &= \frac{A}{h\sqrt{2}}\left(h^2\sigma+\frac{1}{1-Fr^2}\right)\times\zeta_1^{\infty}, \end{aligned} \tag{4.20}$$

where ζ_1^{∞} is the leading wave approximation at the leading order (4.7). The term in rounded brackets is positive for small Froude numbers, thus ζ_G^{∞} causes the amplitude

of the leading wave to increase. This second-order contribution depends on three main parameters: (i) the ratio of disturbance height (or wave amplitude scale) to offshore water depth A/h; (ii) the Froude number Fr; and (iii) the ratio between water depth h and bed perturbation length scale $1/\sqrt{\sigma}$. Therefore, the second-order solution forced at the free surface is valid so long as the ratio A/h and $h\sqrt{\sigma}$ are both small and $Fr \ll 1$, i.e. away from the critical speed.

In the landslide region, a different approximation is required. We write $\zeta_G = \zeta_G^s + \zeta_G^w$, where the superscripts refer to the static and oscillatory components in C. We obtain

$$\begin{aligned}\zeta_G^s &= \frac{A^2u^2}{8h\sqrt{2\pi\sigma}(1-Fr^2)}\int_{-\infty}^{\infty}\frac{\exp(\mathrm{i}kX - k^2/(8\sigma))k^2[4+h^2(1-Fr^2)(k^2+4\sigma)]}{(k^2u^2-\omega^2)\cosh(kh)}\mathrm{d}k \\ &\simeq -\frac{f^2Fr^2}{h(1-Fr^2)}\left(h^2\sigma+\frac{1}{1-Fr^2}\right) = \frac{f}{h}\left(h^2\sigma+\frac{1}{1-Fr^2}\right)\times\zeta_1^s, \end{aligned} \tag{4.21}$$

in which we have adopted an approximation for $k \sim 0$ because of the exponential term $\exp\{-k^2/(8\sigma)\}$. Therefore, the effect of ζ_G^s is to increase the depth trough; indeed the latter is proportional to the square of landslide shape f^2 and increases with Fr.

The second and third terms in C represent the oscillatory component leading to ζ_G^w, which is investigated by applying the stationary phase method as follows:

$$\begin{aligned}\zeta_G^w &\simeq -\frac{A^2uk_0\exp(-k_0^2/(8\sigma))[4+h^2(1-Fr^2)(k_0^2+4\sigma)]}{8\sqrt{2\pi\sigma}h(1-Fr^2)(k_0u-\omega_0)\cosh(k_0h)} \\ &\quad\times\cos[k_0x-\omega_0t+\frac{\pi}{4}]\sqrt{\frac{2\pi}{t\left|\omega_0''\right|}} \\ &= \frac{A\exp(k_0^2/(8\sigma))}{h\sqrt{2}}\left(\frac{1}{1-Fr^2}+\frac{h^2(k_0^2+4\sigma)}{4}\right)\times\zeta_1^w, \end{aligned} \tag{4.22}$$

which is in phase with ζ_1^w (4.10) and so makes a positive contribution. Note that for $k_0 \to 0$ we recover the same term multiplying ζ_1^∞ in (4.20).

4.4. *Second-order term ζ_F*

As is demonstrated in the following section, the term ζ_F is characterised by narrow fluctuations between the leading waves and the landslide region. Given that these oscillations occur along the x-coordinate we expect that among all the forcing terms included in F, those including the x-derivatives provide the most significant contributions. For this reason, we focus solely on the behaviour of $\Phi_x\zeta_x$ and investigate how this term affects the second-order component ζ_F.

From (4.9)–(4.10), we note that away from the leading waves, the spatial derivative of the free surface indicates that it is composed of a stationary shape moving with the bed deformation and an oscillating part as follows:

$$\zeta_{1_x} \simeq \frac{2\sigma XfFr^2}{1-Fr^2} + \frac{Au}{\sqrt{2\sigma t\left|\omega_0''\right|}}\frac{k_0^2\exp(-k_0^2/(4\sigma))}{(k_0u-\omega_0)\cosh(k_0h)}\sin\left(k_0x-\omega_0t+\frac{\pi}{4}\right) = \zeta_{1_x}^s + \zeta_{1_x}^w. \tag{4.23}$$

Similarly, the velocity potential derivative Φ_{1_x} is approximated by

$$\Phi_{1_x} \simeq -\frac{uf}{h(1-Fr^2)} - \frac{Aug}{\sqrt{2\sigma t\,|\omega_0''|}} \frac{k_0^2\,\mathrm{e}^{-k_0^2/(4\sigma)}}{(k_0u-\omega_0)\,\omega_0\cosh(k_0h)} \cos\left(k_0x-\omega_0t+\frac{\pi}{4}\right)$$
$$= \Phi_{1_x}^s + \Phi_{1_x}^w. \tag{4.24}$$

Therefore the corresponding free-surface elevation ζ_F reads

$$\zeta_F(x,t) \simeq -\frac{1}{\pi}\int_0^t\int_{-\infty}^{\infty}\int_{-\infty}^{\infty} \zeta_{1_\xi}\Phi_{1_\xi}\exp(-\mathrm{i}k(\xi-x))\cos\omega(\tau-t)\,\mathrm{d}\xi\,\mathrm{d}k\,\mathrm{d}\tau. \tag{4.25}$$

The forcing component $\zeta_{1_\xi}^w\Phi_{1_\xi}^w$ in the integral above, decays as $O(t^{-1})$, i.e. much faster than $\zeta_{1_\xi}^s\Phi_{1_\xi}^s$, $\zeta_{1_\xi}^w\Phi_{1_\xi}^s$ and $\zeta_{1_\xi}^s\Phi_{1_\xi}^w$, and so makes a negligible contribution.

Recalling that $\zeta_1 = \zeta_{1_x}^s + \zeta_{1_x}^w$, accordingly we write $\zeta_F = \zeta_F^s + \zeta_F^{sw}$, where the superscripts indicate the contributions of static ($\zeta_{1_\xi}^s\Phi_{1_\xi}^s$) and product between oscillating and static components ($\zeta_{1_\xi}^s\Phi_{1_\xi}^w$; $\zeta_{1_\xi}^w\Phi_{1_\xi}^s$), respectively, to the second-order term (4.25). The contribution of $\zeta_{1_\xi}^s\Phi_{1_\xi}^s$ yields

$$\zeta_F^s \simeq \frac{2A^2gu^3\sigma}{\pi(gh-u^2)^2}\int_0^t\int_{-\infty}^{\infty}\int_{-\infty}^{\infty}\exp(-\mathrm{i}k(\xi-x)-2(\xi-u\tau)^2\sigma)$$
$$\times(\xi-\tau u)\cos[\omega(\tau-t)]\mathrm{d}\xi\,\mathrm{d}k\,\mathrm{d}\tau$$
$$= \frac{Au^2g}{2\pi\sqrt{2}(u^2-gh)^2}\int_{-\infty}^{\infty}\exp(\mathrm{i}kx+k^2/(8\sigma))C(k,t)\,\mathrm{d}k. \tag{4.26}$$

If we focus attention on the leading wave, the primary contribution is given by $k\sim 0$, hence the integral above can be approximated as

$$\zeta_F^{s,\infty} \simeq \frac{A^2u^3g\sqrt{\pi}}{2\pi\sqrt{2\sigma}(u^2-gh)^2(\sqrt{gh}-u)}$$
$$\times Re\int_0^{\infty}\cos(kx-\omega t)\mathrm{d}k = \frac{AFr^2}{\sqrt{2}h(Fr^2-1)^2}\times\zeta_1^{\infty}, \tag{4.27}$$

which causes the amplitude of the leading wave to increase. The second-order contribution of (4.27) depends on two main parameters: (i) the ratio of disturbance height (or wave amplitude scale) to offshore water depth A/h; and (ii) the Froude number Fr. Therefore, the second-order solution forced at the free surface is valid so long as the ratio A/h is small and $Fr<1$, i.e. away from the critical speed. Note also that for small Froude numbers (4.27) is much smaller than the second-order leading wave component ζ_G^{∞} (4.20). In this work $Fr\ll 1$ and so $\zeta_F^{s,\infty}$ makes a small contribution to the leading wave behaviour. If we now focus on the disturbance region, performing a similar analysis as in § 4.2 on expression (4.26) yields $\zeta_F^s = \zeta_F^{s,s} + \zeta_F^{s,w}$, where

$$\zeta_F^{s,s} \simeq \frac{A^2u^4g}{2\sqrt{2}(u^2-gh)^3\sqrt{\sigma\pi}}\int_{-\infty}^{\infty}\exp([\mathrm{i}kX-k^2/(8\sigma)])\mathrm{d}k = -\frac{f^2Fr^4}{h(1-Fr^2)^3}. \tag{4.28}$$

Therefore, the effect of $\zeta_F^{s,s}$ is to increase the depth of the trough and to reduce its width. This term is mainly related to the shape f and speed u of the moving deformation and gives insignificant results when $Fr\ll 1$.

It remains to investigate the term $\zeta_F^{s,w}$ given by the remaining contribution to C. From (4.26), the stationary phase method gives

$$\zeta_F^{s,w} = \frac{AFr^2 \exp(k_0^2/(8\sigma)) \cosh(k_0 h)}{h\sqrt{2}(1-Fr^2)} \times \zeta_1^w, \tag{4.29}$$

which is small for bed deformation speeds far from the shallow-water wave celerity. Note that $\zeta_F^{s,w}$ is in phase with the leading-order waves ζ_1^w (4.10), and so its effect is to increase their amplitude in the vicinity of the bed deformation.

The effect of $\zeta_{1_x}^w$ and $\Phi_{1_x}^w$ on the second-order term ζ_F yields

$$\begin{aligned}\zeta_F^{sw}(x,t) = {} & \frac{A^2 u}{\pi\sqrt{2\sigma}(1-Fr^2)} \\ & \times \int_0^t \int_{-\infty}^{\infty}\int_{-\infty}^{\infty} \frac{k_0^2 \cos[\omega(\tau-t)] \exp(-\mathrm{i}k(\xi-x) - \sigma(\xi-u\tau)^2 - k_0^2/(4\sigma))}{\sqrt{\tau\,|\omega_0''|}\,(k_0 u - \omega_0)\cosh(k_0 h)} \\ & \times \left[\frac{2\sigma(\xi-u\tau)Fr^2 g}{\omega_0}\cos\left(k_0\xi - \omega_0\tau + \frac{\pi}{4}\right) + \frac{u}{h}\sin\left(k_0\xi - \omega_0\tau + \frac{\pi}{4}\right)\right] \mathrm{d}\xi\,\mathrm{d}k\,\mathrm{d}\tau.\end{aligned} \tag{4.30}$$

The latter is more complicated than (4.26) because k_0 and ω_0 depend on space and time. To obtain an approximate solution of this integral at large distance, we first derive the approximate location of the stationary point by noting that the exponential term in the integrals concentrates effects in the landslide region $(\xi - u\tau)$. This provides k_0 and ω_0'' expressed as (4.11*a*,*b*). Then we solve the integrals in τ and ξ, and expand the frequency ω about $k \sim 0$ except the phase function $\mathrm{e}^{\mathrm{i}\omega t}$. This yields

$$\begin{aligned}\zeta_F^{sw}(x,t) \simeq {} & \frac{\mathrm{i}A^2 g k_0^2 Fr^2 \exp\left(-\dfrac{k_0^2}{2\sigma}\right)}{4\sigma\sqrt{2\,|\omega_0''|\,(\omega_0 - k_0 u)}(1-Fr^2)\omega_0\cosh(k_0 h)} \\ & \times \{\mathrm{Erf}[(1+\mathrm{i})\chi] + \mathrm{Erf}[(\mathrm{i}-1)\chi]\}\int_{-\infty}^{\infty}\exp(\mathrm{i}(kx-\omega t))\,\mathrm{d}k, \quad \chi = \frac{\sqrt{t(\omega_0 - k_0 u)}}{\sqrt{2}},\end{aligned} \tag{4.31}$$

where Erf denotes the error function. Using the series expansion (7.1.29) in Abramowitz & Stegun (1972), we decompose the Erf into real and imaginary parts, giving

$$\begin{aligned}\zeta_F^{sw}(x,t) = {} & -\frac{A^2 g k_0^2 Fr^2 \exp\left(-\dfrac{k_0^2}{2\sigma}\right)}{4\sigma\sqrt{2\,|\omega_0''|\,(\omega_0 - k_0 u)}(1-Fr^2)\omega_0\cosh(k_0 h)}\mathrm{e}^{-\chi^2} \\ & \times \left[\frac{\sin(2\chi^2)}{2\pi\chi} + \frac{2}{\pi}\sum_{n=1}^{\infty}\frac{\mathrm{e}^{-(n^2/4)}(2\chi\cosh(n\chi)\sin(2\chi^2) + n\sinh(n\chi)\cos(2\chi^2))}{n^2+4\chi^2}\right]\end{aligned}$$

$$\times \int_{-\infty}^{\infty} \exp\left(\mathrm{i}\left(kx-\omega t\right)\right) \mathrm{d}k \simeq \frac{Agu \exp\left(-\dfrac{k_0^2}{4\sigma}\right) \sin\left(\dfrac{\pi}{4}+2\chi^2\right)}{4\pi^2 h\sqrt{2}(1-Fr^2)\chi\,(gh)^{1/4}} \sqrt{\frac{k_0(1-Fr)}{\sigma\left|\omega_0''\right|}} \times \zeta_1^w. \tag{4.32}$$

Since χ is proportional to $\sqrt{t}$ and ζ_1^w decays as $O(t^{-1/2})$, the above expression decays as $O(t^{-1})$, i.e. it decreases faster than the wave oscillations at leading order (4.10); $\zeta_F^{sw}(x,t)$ is also responsible for a modulation of the wave trough in the bed deformation region with frequency

$$2\chi^2/t = \omega_0 - k_0 u \simeq k_0\left(\sqrt{gh}-u\right) = \sqrt{\frac{2g}{h}}\,(1-Fr)^{3/2}. \tag{4.33}$$

This is a peculiarity of nonlinear theory whose effects will be discussed in the next section. We point out that similar qualitative behaviour was also observed experimentally by Whittaker *et al.* (2015).

4.5. *Second-order term B*

As also demonstrated in the next section, the behaviour of the term B resembles a propagating narrow trough of constant shape and speed u. This means that terms including oscillating components make negligible contributions. Therefore,

$$\begin{aligned} B &\simeq -\frac{1}{\epsilon g}\left[\frac{1}{2}(\Phi_{1_x}^{s^2}+\zeta_{1_t}^{s^2})+\Phi_{1_{zt}}^{s}\zeta_1^s\right] \\ &= \left\{\frac{1}{2h(1-Fr^2)}+\frac{2u^2\sigma^2(1-Fr^2)X^2}{gFr}\right. \\ &\quad \left.+2h\sigma Fr^2[1+4tux-2\sigma(x^2+u^2t^2)]\right\}\times\zeta_1^s f, \end{aligned} \tag{4.34}$$

in which we utilise the wave trough approximation at leading order ζ_1^s expressed by (4.9); f concentrates the effects in the landslide region $X\sim 0$, and so for small Froude numbers $Fr \ll 1$ and $X \ll 1$ expression (4.34) can be crudely approximated as

$$B \simeq \frac{f}{2h(1-Fr^2)} \times \zeta_1^s. \tag{4.35}$$

Equation (4.35) represents a small wave trough propagating with the bed deformation. Since $f \sim O(A) \ll h$, away from the critical speed the ratio in the latter expression is much smaller than unity, and is of order ϵ. This is in agreement with the perturbation expansion in terms of ϵ. Note that

$$\lim_{Fr\to 0}\frac{B}{\zeta_G^s} = \frac{1}{2(h^2\sigma+1)}, \tag{4.36}$$

with ζ_G^s given by (4.21). Therefore, for large ratio between sea depth h and bed slide length scale $1/\sqrt{\sigma}$, B becomes much smaller than ζ_G^s, and so exerts a minor effect at second order.

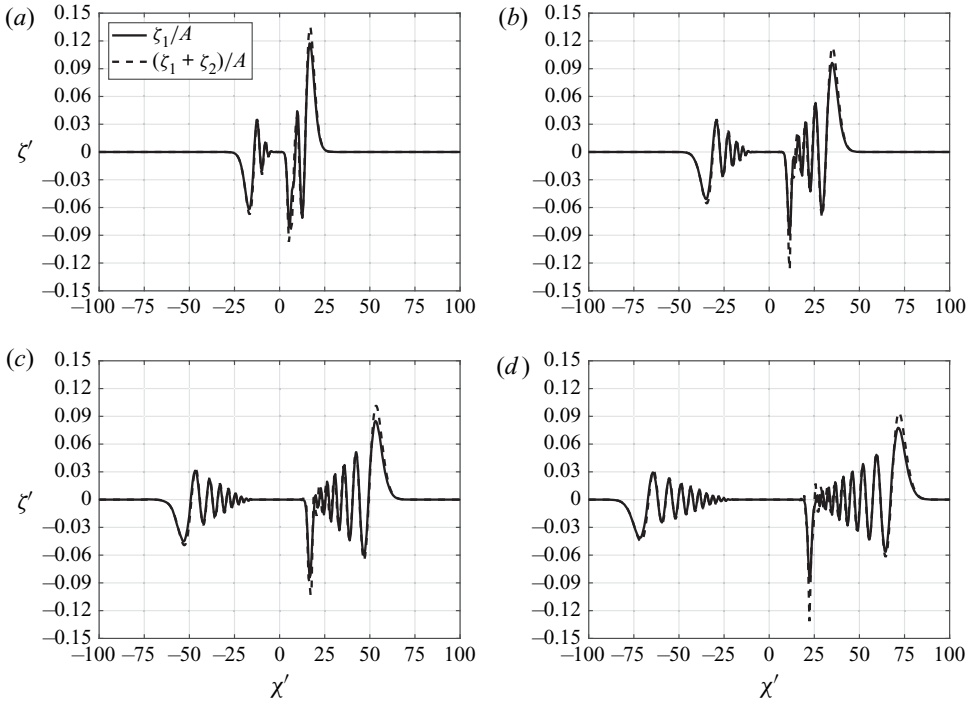

Figure 3. First- and second-order non-dimensional free-surface elevation profiles $\zeta' = \zeta/A$ vs $\chi' = x/h$ at non-dimensional times: (*a*) $\tau' = 18.71$, (*b*) $\tau' = 37.43$, (*c*) $\tau' = 56.14$ and (*d*) $\tau' = 74.85$. Values of channel depth and slide amplitude are $h = 0.175$, $A = 0.026$ m, whereas the bed slide Froude number is $Fr = 0.3$.

5. Results and discussion

5.1. *Linear and weakly nonlinear model results*

We now consider the same channel flume and moving disturbance geometry analysed in § 3, with larger Froude number $Fr = 0.3$, equivalent to bed slide speed $u = 0.393\,\mathrm{m\,s^{-1}}$. For a better understanding of the physical phenomenon, we define the following non-dimensional variables:

$$\chi' = \frac{x}{h}, \quad \tau' = t\sqrt{\frac{g}{h}}. \tag{5.1a,b}$$

Figure 3 presents snapshots of both the linear and nonlinear solutions at times $t = [2.5, 5, 7.5, 10]$ s, corresponding to $\tau' = [18.71, 37.43, 56.14, 74.85]$. The free-surface elevation components are evaluated by solving the complete integrals in § 2. The second-order leading wave elevation is larger than that evaluated according to leading-order theory, whereas over the moving bed deformation the free surface exhibits a more pronounced pulsation in the nonlinear solution, unlike the linearised approximation. The leftwards propagating wave is not as strongly affected by nonlinear dynamics as the wave propagating in the direction of the disturbance.

Figure 4 shows the second-order components: the bed-forced solution ζ_G, the free-surface-forced solution ζ_F, and the second-order component B arising from the first-order solution.

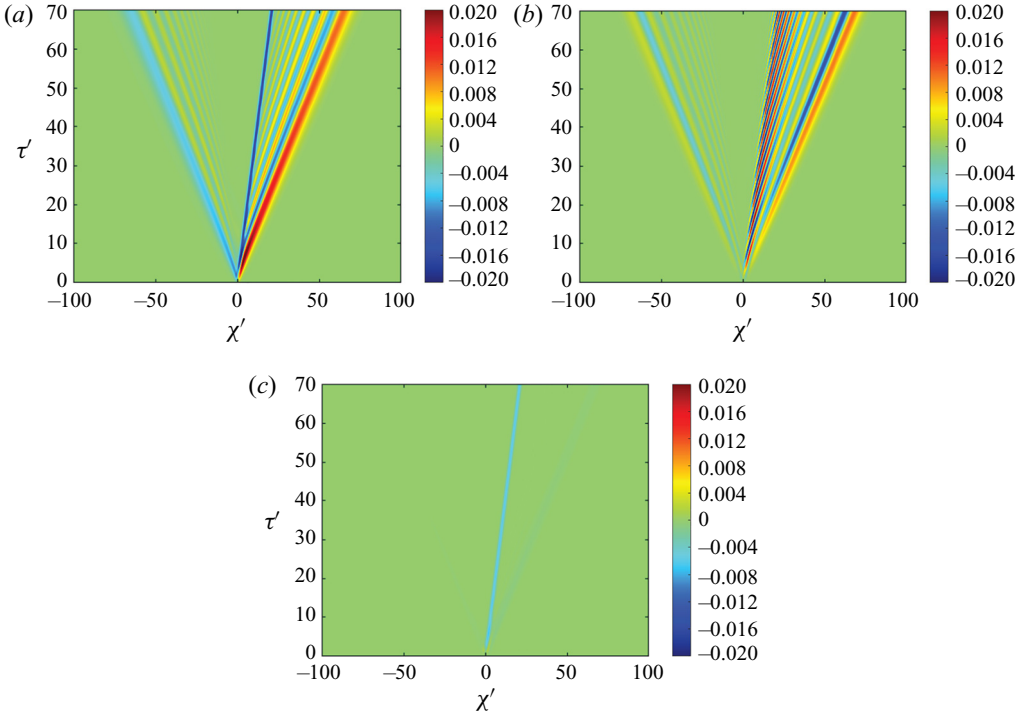

Figure 4. Spatio-temporal behaviour of second-order components vs non-dimensional variables $\chi' = x/h$, $\tau' = t\sqrt{g/h}$; (*a*) ζ_G/A, (*b*) ζ_F/A and (*c*) B/A.

Comparison of the numerical values between figures 3–4(*a*) reveals that the behaviour of the ζ_G component is similar to that of the leading-order wave. This validates the approximated theoretical expressions in § 4.3.

Here, ζ_F exhibits a relatively short wavelength wavy pattern in the bed deformation region, but seems to have only a minor effect on the leading wave maximum value, especially at low Froude numbers. We remark that our theory is valid so long as the Froude number is not close to unity. As shown in § 4.4, the term ζ_F causes narrow oscillations in the bed deformation region and this explains why the trough presents fast oscillations at second order. This has also been observed in experiments by Whittaker *et al.* (2015) in the bed slide region (see figures 5–7–10 of the mentioned work).

Finally, figure 4(*c*) shows that the behaviour of B is mainly characterised by a small trough propagating with the bed deformation. Note also that the value of ζ_G is smaller than ζ_F, even though their contributions are of the same order of magnitude. This is in agreement with the asymptotic expansions of § 4.5.

5.2. *Weakly nonlinear and dispersive effects on leading wave behaviour*

In this section we examine the effects of second-order contributions and wave dispersion on the behaviour of propagating waves in the region $x \sim t\sqrt{gh}$. For later convenience, we first define the following non-dimensional variables $\xi' = x' - \tau'$, where ξ' denotes a non-dimensional moving coordinate. In dimensional variables $\xi = \xi' h = x - t\sqrt{gh}$ represents the distance from a wave front propagating in shallow water. Figure 5 shows the behaviour of the non-dimensional leading wave amplitude predicted by second-order

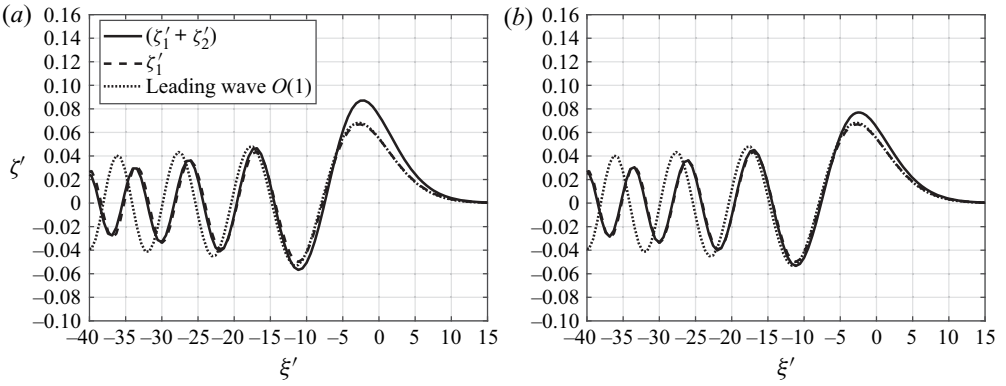

Figure 5. Effect of disturbance amplitude A on leading waves at $\tau' = 120$; (a) $A = 0.026$ m and (b) $A = 0.013$ m. Second-order contributions affect mainly the first leading wave crest, whereas wave dispersion shortens the wavelength of subsequent oscillations with respect to the leading wave approximation (4.7).

theory, leading-order theory and the leading wave approximation (4.7) as a function of non-dimensional distance ξ' at non-dimensional time $\tau' = 120$. The moving bed geometry is the same as in the previous section except for its amplitude. Specifically, figure 5(a) refers to a case with disturbance amplitude $A = 0.026$ m, whereas figure 5(b) refers to a case with smaller amplitude $A = 0.013$ m. Figures 5(a) and 5(b) show that the main effect of the second-order contributions is to increase the leading wave crest height and the following trough depth. Far from the first leading waves, however, the free-surface elevation predicted at leading order is almost coincident with that predicted at second order. In this region, the wave steepness and the effect of nonlinearity both decrease, hence the influence of quadratic forcing terms becomes small.

Figure 5(a) shows that a larger disturbance amplitude affects the first oscillations and tends to increase their amplitude. In particular, the difference between leading-order and second-order oscillations increases almost proportionally with A. This is in agreement with the assumption that the wave steepness is a small parameter ϵ.

As far as dispersion is concerned, note that the trailing waves in the dispersive solution shorten faster than predicted by the weakly dispersive leading wave approximation (4.7). To explain this behaviour we refer to the method of stationary phase, recalling that an observer far from the wave front and moving at speed $C_g = \omega'(k_0)$ sees a train of sinusoidal waves with fixed wavenumber k_0. Since (4.7) is derived using the Boussinesq approximation (4.3) instead of the full dispersion relation, we find that $C_{Boussinesq} < C_g$. As a consequence, the Boussinesq approximation fails to predict the correct time of arrival of trailing crests and troughs.

Now let us consider the influence of the disturbance length. The behaviour of the leading waves for two different disturbance lengths and fixed $A = 0.026$ m is shown in figure 6. Figures 6(a) and 6(b) refer to $\sigma = 19/2$ and $\sigma = 19 \times 2\,\mathrm{m}^{-2}$. These correspond, respectively, to disturbance lengths increased and divided by a factor $\sqrt{2}$, compared with the previous cases. The leading wave approximation captures well the behaviour of the first leading waves at first order, whereas second-order effects tend to increase wave amplitude. The main differences lie in the behaviour of the oscillations behind the front. As the disturbance length increases, the spatial decay of the oscillation becomes more pronounced than that predicted by (4.7). This is because the disturbance is longer, and so more time τ' is needed for the leading waves to exhibit asymptotic behaviour. The opposite occurs in

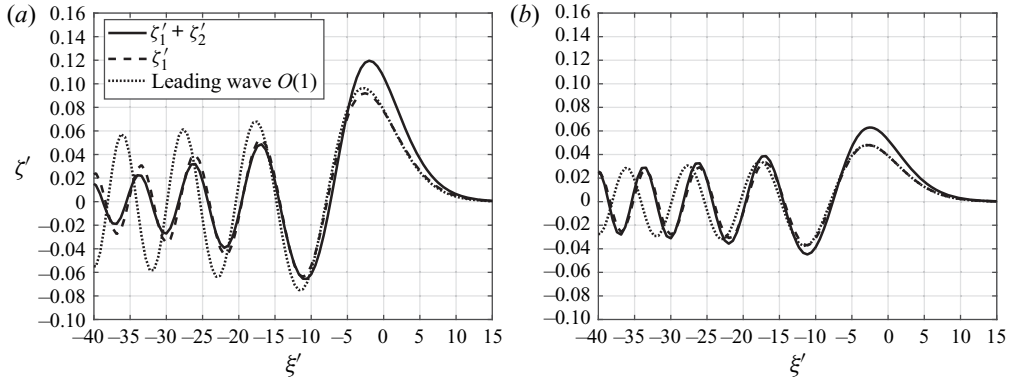

Figure 6. Effect of disturbance length on leading waves at $\tau' = 120$. (*a*) $\sigma = 19/2\,\mathrm{m}^{-2}$ and (*b*) $\sigma = 19 \times 2\,\mathrm{m}^{-2}$. As in figure 5, the second-order contributions affect the first leading wave height, and subsequent oscillations are shorter than (4.7). Note that larger disturbances increase the spatial decay of the wave pattern behind the wave front.

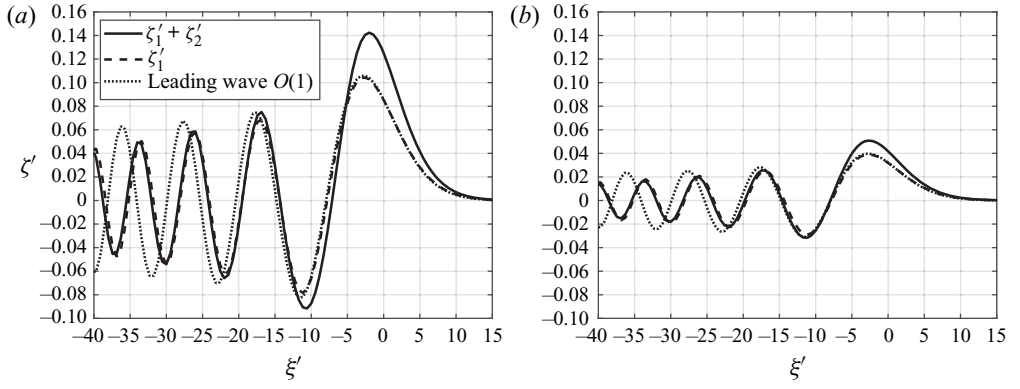

Figure 7. Effect of disturbance speed on leading waves for $\tau' = 120$; (*a*) $Fr = 0.4$ and (*b*) $Fr = 0.2$. The spatial decay is similar to that described by (4.7), and nonlinearity becomes progressively significant as the Froude number increases.

the case shown in figure 6(*b*) where the spatial decay is smaller but the nonlinear effects are more important because of the increase in disturbance steepness.

Figure 7 highlights the effect of seabed deformation speed on the leading waves. Specifically, figures 7(*a*) and 7(*b*) show the behaviour of ζ' for Froude numbers $Fr = 0.4$ and $Fr = 0.2$. By comparing figures 5(*a*) and 7 we observe that the free-surface elevation at second order increases with disturbance speed, while the spatial decay of oscillations behind the first leading waves remains well described by the approximation (4.7).

Finally, figure 8 summarises all the foregoing results and shows the ratio of the second-order to the leading-order contribution $(\zeta_1 + \zeta_2)/\zeta_1$, evaluated according to the maximum elevation of the leading wave for several disturbance sizes and fixed non-dimensional time $\tau' = 80$. The figure shows that nonlinear effects increase with σ, i.e. with disturbance steepness and the slide height A.

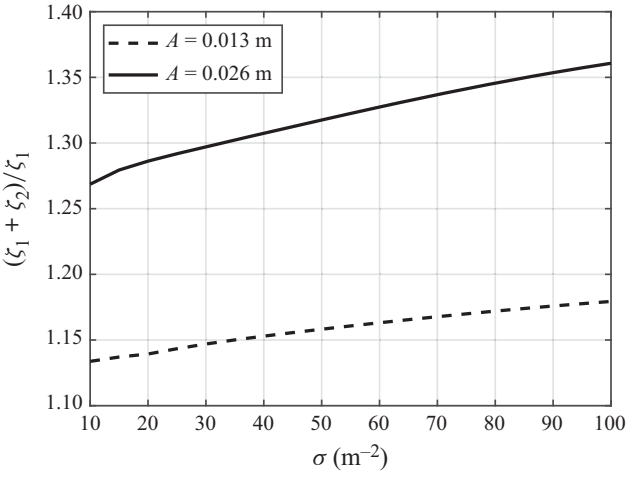

Figure 8. Ratio of maximum elevations of the leading wave $(\zeta_1 + \zeta_2)/\zeta_1$ evaluated from second- and leading-order theory. This figure shows that second-order effects increase with the bed slide steepness and height A.

6. Conclusions

We investigated the nonlinear hydrodynamics of dispersive transient waves generated by a moving disturbance over a flat bed. This allowed us to elucidate the role of higher-order components in shaping the wave field. The analytical model is solved by applying a perturbation expansion to the governing equations. This yields a cascade of linearised b.v.p.s, each of which is solved by means of the exponential Fourier transform in space. We show that the second-order problem is forced by three main contributions: (i) nonlinearity at the free surface; (ii) bed deformation steepness; and (iii) quadratic products given by the solution at leading order. Their effect is to increase the free-surface amplitude and to trigger oscillations in the trough above the disturbance. This explains earlier experimental observations by Whittaker *et al.* (2015).

A parametric analysis of the system reveals that the first leading waves of the wave train exhibits nonlinear non-dispersive behaviour, whereas closer to the tail the oscillations are satisfactorily predicted by linear dispersive theory. The Boussinesq leading wave approximation works well for the first crest, but predicts incorrect times of arrival for the trailing waves. As expected, increases to the amplitude and speed of the bed deformation magnify nonlinear effects.

The analytical model is validated by comparison with experimental results. Very good agreement is found, given the complexity of the geometry and the impulse generated by the instantaneous bed deformation motion.

We remark that the mathematical model is based on a simplified assumption of bed deformation propagation at low Froude number. As Fr increases, the weakly nonlinear theory starts to overpredict the wave amplitude, and other approaches are necessary. This aspect is rather important, and worth further investigation.

The present study has considered a simplified bathymetry, where the bed disturbance moves over an otherwise flat surface, reproducing the experimental layout of Whittaker *et al.* (2015). Based on our results, and the scales involved in the phenomenon, it is reasonable to expect very similar results on a mildly sloping bathymetry, i.e. for a landslide. This is because the horizontal scale of motion, proportional to the landslide length, is usually much greater than the vertical one, proportional to the landslide height.

However, our results may not necessarily hold in the presence of steep depth contours, such as cliffs and submarine canyons. Also, we assumed a two-dimensional geometry and neglected additional three-dimensional effects, such as edge waves, which can become dominant in the presence of trapping structures like beaches and continental shelves (Sammarco & Renzi 2008; Renzi & Sammarco 2012, 2016).

Finally, asymptotic analyses are performed in the simplified assumption of a Gaussian bed slide moving over a rigid horizontal seabed. More complicated seabed profiles such as tensile faults (Okada 1985, 1992) are worth future investigation.

All the aforementioned aspects add levels of complexity that require the use of large-scale numerical and experimental models. The results obtained herein for idealised geometries contribute to our understanding of the hydrodynamics of dispersive landslide tsunamis affected by higher-order contributions.

Acknowledgements. The authors are grateful to the referees for their constructive and helpful comments.

Declaration of interests. The authors report no conflict of interest.

Author ORCIDs.
S. Michele https://orcid.org/0000-0002-4082-6929;
A.G.L. Borthwick https://orcid.org/0000-0001-6053-7764.

Appendix A. Leading-order velocity potential, free-surface elevation and their derivatives

Components of the second-order forcing term F, evaluated on the free surface $z = 0$, are expressed as

$$\Phi_1 = -\frac{g}{2\pi}\int_{-\infty}^{\infty}\frac{\mathrm{e}^{\mathrm{i}kx}}{\omega\cosh(kh)}S\,\mathrm{d}k, \quad \Phi_{1_x} = -\frac{\mathrm{i}g}{2\pi}\int_{-\infty}^{\infty}\frac{k\,\mathrm{e}^{\mathrm{i}kx}}{\omega\cosh(kh)}S\,\mathrm{d}k, \tag{A1a,b}$$

$$\Phi_{1_z} = -\frac{1}{2\pi}\int_{-\infty}^{\infty}\frac{\omega\,\mathrm{e}^{\mathrm{i}kx}}{\cosh(kh)}S\,\mathrm{d}k + \frac{1}{2\pi}\int_{-\infty}^{\infty}\frac{\hat{W}\,\mathrm{e}^{\mathrm{i}kx}}{\cosh(kh)}\mathrm{d}k, \tag{A2}$$

$$\Phi_{1_{zz}} = -\frac{1}{2\pi}\int_{-\infty}^{\infty}\frac{k\omega\,\mathrm{e}^{\mathrm{i}kx}}{\sinh(kh)}\mathrm{d}k, \tag{A3}$$

$$\Phi_{1_{tz}} = -\frac{1}{2\pi}\int_{-\infty}^{\infty}\frac{\omega^2\,\mathrm{e}^{\mathrm{i}kx}}{\cosh(kh)}C\,\mathrm{d}k + \frac{1}{2\pi}\int_{-\infty}^{\infty}\frac{\hat{W}_t\,\mathrm{e}^{\mathrm{i}kx}}{\cosh(kh)}\mathrm{d}k, \tag{A4}$$

$$\Phi_{1_{ttz}} = -\frac{1}{2\pi}\int_{-\infty}^{\infty}\frac{\omega^2\,\mathrm{e}^{\mathrm{i}kx}}{\cosh(kh)}[-\omega S + W]\,\mathrm{d}k + \frac{1}{2\pi}\int_{-\infty}^{\infty}\frac{\hat{W}_{tt}\,\mathrm{e}^{\mathrm{i}kx}}{\cosh(kh)}\mathrm{d}k, \tag{A5}$$

$$\zeta_1 = \frac{1}{2\pi}\int_{-\infty}^{\infty}\frac{\mathrm{e}^{\mathrm{i}kx}}{\cosh(kh)}C\,\mathrm{d}k, \quad \zeta_{1x} = \frac{\mathrm{i}}{2\pi}\int_{-\infty}^{\infty}\frac{k\,\mathrm{e}^{\mathrm{i}kx}}{\cosh(kh)}C\,\mathrm{d}k, \tag{A6a,b}$$

and the components for G at the bed $z = -h$

$$\Phi_{1_{zz}} = -\frac{g}{2\pi}\int_{-\infty}^{\infty}\frac{k^2\,\mathrm{e}^{\mathrm{i}kx}}{\omega\cosh^2(kh)}S\,\mathrm{d}k - \frac{1}{2\pi}\int_{-\infty}^{\infty}\frac{\hat{W}\omega^2\,\mathrm{e}^{\mathrm{i}kx}}{g}\mathrm{d}k, \tag{A7}$$

$$\Phi_{1_x} = -\frac{\mathrm{i}g}{2\pi}\int_{-\infty}^{\infty}\frac{k\,\mathrm{e}^{\mathrm{i}kx}}{\omega\cosh^2(kh)}S\,\mathrm{d}k - \frac{\mathrm{i}}{2\pi g}\int_{-\infty}^{\infty}\frac{\hat{W}\omega^2\,\mathrm{e}^{\mathrm{i}kx}}{k}\mathrm{d}k. \tag{A8}$$

References

Abramowitz, M. & Stegun, I. 1972 *Handbook of Mathematical Functions*. Dover.

Bender, C.M. & Orszag, S.A. 1999 *Advanced Mathematical Methods for Scientists and Engineers*. Springer.

Capone, T., Panizzo, A. & Monaghan, J. 2010 SPH modelling of water waves generated by submarine landslides. *J. Hydraul Res.* **48**, 80–84.

Cecioni, C. & Bellotti, G. 2010 Modeling tsunamis generated by submerged landslides using depth integrated equations. *Appl. Ocean Res.* **32**, 343–350.

Couston, L.-A., Mei, C.C. & Alam, M.-R. 2015 Landslide tsunamis in lakes. *J. Fluid Mech.* **772**, 784–804.

Dalphin, J. & Barros, R. 2019 Optimal shape of an underwater moving bottom generating surface waves ruled by a forced Korteweg-de Vries equation. *J. Optim. Theor. Applics.* **180**, 574–607.

Debnath, L. 1994 *Nonlinear Water Waves*. Academic.

Di Risio, M., Bellotti, G., Panizzo, A. & Girolamo, P.D. 2009 Three-dimensional experiments on landslide generated waves at a sloping coast. *Coast. Engng* **56**, 659–671.

Enet, F. & Grilli, S.T. 2007 Experimental study of tsunami generation by three-dimensional rigid underwater landslides. *ASCE J. Waterway Port Coastal Ocean Engng* **133**, 442–454.

Fraser, S., Raby, A., Pomonis, A., Goda, K., Chian, S.C., Macabuag, J., Offord, M., Saito, K. & Sammonds, P. 2013 Tsunami damage to coastal defences and buildings in the March 11th 2011 M w 9.0 Great East Japan earthquake and tsunami. *Bull. Earthq. Engng* **11**, 205–239.

Goda, K., Mori, N., Yasuda, T., Prasetyo, A., Muhammad, A. & Tsujio, D. 2019 Cascading geological hazards and risks of the 2018 Sulawesi Indonesia earthquake and sensitivity analysis of tsunami inundation simulations. *Front. Earth Sci.* **7**, 261.

Grilli, S.T. & Watts, P. 2005 Tsunami generation by submarine mass failure. I. Modeling, experimental validation, and sensitivity analyses. *ASCE J. Waterway Port Coastal Ocean Engng* **131**, 283–297.

Hammack, J.L. 1973 A note on tsunamis: their generation and propagation in an ocean of uniform depth. *J. Fluid Mech.* **60**, 769–799.

Heller, V., Bruggeman, M., Spinneken, J. & Rogers, B. 2016 Composite modelling of subaerial landslide–tsunamis in different water body geometries and novel insight into slide and wave kinematics. *Coast. Engng* **109**, 20–41.

Kanoglou, U. & Synolakis, C.E. 2015 Tsunami dynamics, forecasting, and mitigation. In *Coastal and Marine Hazards, Risks, and Disasters* (ed. J.T. Ellis & D.J. Sherman), pp. 15–57. Elsevier.

Kirby, J.T. 2016 Boussinesq models and their application to coastal processes across a wide range of scales. *ASCE J. Waterway Port Coastal Ocean Engng* **142** (6), 03116005.

Lee, S.-J., Yates, G.T. & Wu, T.Y. 1989 Experiments and analyses of upstream-advancing solitary waves generated by moving disturbances. *J. Fluid Mech.* **199**, 569–593.

Levin, B.W. & Nosov, M.A. 2016 *Physics of Tsunamis*. Springer.

Li, H., Jin, Y.C. & Tai, Y.C. 2020 A numerical and experimental investigation of wave generated by submerged landslides. *Ocean Engng* **218**, 108203.

Liu, P.L.-F. & Mei, C.C. 2003 Analytical solutions for forced long waves on a sloping beach. *J. Fluid Mech.* **478**, 101–109.

Lynett, P. & Liu, P.L.-F. 2005 A numerical study of the run-up generated by three-dimensional landslides. *J. Geophys. Res.* **110**, C03006.

Ma, G., Shi, F. & Kirby, J.T. 2012 Shock-capturing non-hydrostatic model for fully dispersive surface wave processes. *Ocean Model.* **43–44**, 22–35.

Madsen, P.A. & Hansen, A.B. 2012 Transient waves generated by a moving bottom obstacle: a new near-field solution. *J. Fluid Mech.* **697**, 237–272.

Mei, C.C., Stiassnie, M. & Yue, D.K.-P. 2005 *Theory and Application of Ocean Surface Waves*. World Scientific.

Michele, S. & Renzi, E. 2019 A second-order theory for an array of curved wave energy converters in open sea. *J. Fluids Struct.* **88**, 315–330.

Michele, S., Renzi, E. & Sammarco, P. 2019 Weakly nonlinear theory for a gate-type curved array in waves. *J. Fluid Mech.* **869**, 238–263.

Michele, S., Sammarco, P. & d'Errico, M. 2018 Weakly nonlinear theory for oscillating wave surge converters in a channel. *J. Fluid Mech.* **834**, 55–91.

Okada, Y. 1985 Surface deformation due to shear and tensile faults in a half-space. *Bull. Seismol. Soc. Am.* **75**, 1135–1154.

Okada, Y. 1992 Internal deformation due to shear and tensile faults in a half-space. *Bull. Seismol. Soc. Am.* **82**, 1018–1040.

RENZI, E. 2017 Hydro-acoustic frequencies of the weakly compressible mild-slope equation. *J. Fluid Mech.* **812**, 5–25.

RENZI, E. & SAMMARCO, P. 2010 Landslide tsunamis propagating around a conical island. *J. Fluid Mech.* **650**, 251–285.

RENZI, E. & SAMMARCO, P. 2012 The influence of landslide shape and continental shelf on landslide generated tsunamis along a plane beach. *Nat. Hazards Earth Syst. Sci.* **12**, 1503–1520.

RENZI, E. & SAMMARCO, P. 2016 The hydrodynamics of landslide tsunamis: current analytical models and future research directions. *Landslides* **13**, 1369–1377.

ROMANO, A., BELLOTTI, G. & RISIO, M.D. 2013 Wavenumber–frequency analysis of the landslide-generated tsunamis at a conical island. *Coast. Engng* **81**, 32–43.

SAMMARCO, P. & RENZI, E. 2008 Landslide tsunamis propagating along a plane beach. *J. Fluid Mech.* **598**, 107–119.

SCHÄFFER, H.A. & MADSEN, P.A. 1995 Further enhancements of Boussinesq-type equations. *Coastal Engng* **26**, 1–14.

SUE, L.P., NOKES, R.I. & DAVIDSON, M.J. 2011 Tsunami generation by submarine landslides: comparison of physical and numerical models. *Environ. Fluid Mech.* **11**, 133–165.

WANG, Y., LIU, P.L.-F. & MEI, C.C. 2010 Solid landslide generated waves. *J. Fluid Mech.* **675**, 529–539.

WATTS, P. 2000 Tsunami features of solid block underwater landslides. *ASCE J. Waterway Port Coastal Ocean Engng* **126**, 144–152.

WHITHAM, G.B. 1974 *Linear and Nonlinear Waves*. Wiley.

WHITTAKER, C.J., NOKES, R.I. & DAVIDSON, M.J. 2015 Tsunami forcing by a low Froude number landslide. *Environ. Fluid Mech.* **15**, 1215–1239.

WHITTAKER, C.J., NOKES, R.I., LO, H.-Y., LIU, P.L.-F. & DAVIDSON, M.J. 2017 Physical and numerical modelling of tsunami generation by a moving obstacle at the bottom boundary. *Environ. Fluid Mech.* **17**, 929–958.

WU, T.Y. 1987 Generation of upstream advancing solitons by moving disturbances. *J. Fluid Mech.* **184**, 75–99.

YAVARI-RAMSHE, S. & ATAIE-ASHTIANI, B. 2016 Numerical modeling of subaerial and submarine landslide-generated tsunami waves–recent advances and future challenges. *Landslides* **13**, 1325–1368.